Journal of Materials Chemistry C

PAPER

View Article Online
View Journal | View Issue

Cite this: J. Mater. Chem. C, 2019, 7, 14731

Defect repair for enhanced piezo-phototronic MoS_2 flexible phototransistors†

Pei Lin,[ab] Laipan Zhu,[bc] Ding Li[bc] and Zhong Lin Wang *[bcd]

Received 29th September 2019,
Accepted 21st October 2019

DOI: 10.1039/c9tc05337a

rsc.li/materials-c

The recent emergence of two-dimensional piezoelectric monolayers has provided a powerful platform for exploring the piezo-phototronic effect at the atomic scale, giving rise to multiple new physics and innovative device applications. However, being atomically thin, the piezoelectric properties of these materials are extremely vulnerable to structural defects, which may largely limit their practical use in high performance piezo-phototronics. In this study, we demonstrate the feasibility of piezo-phototronic effect enhancement in chemical vapor deposition grown MoS_2 through sulfur vacancy repair and carrier concentration manipulation. Compared with flexible phototransistors fabricated with the as-grown MoS_2 monolayer, a more prominent piezo-phototronic modulation impact was achieved after defect repair. This improvement originates from improved crystallization and a suppressed free-carrier screening effect in semiconducting MoS_2. Under illumination of 19.1 μW cm^{-2} (532 nm wavelength), a 5.6-fold increase of responsivity is demonstrated when a 0.42% uniaxial tensile strain is applied and the optimized photoresponsivity reaches up to 339.2 A W^{-1}. This structure–property relationship research could advance our fundamental understanding of the piezo-phototronic effect in 2D ultrathin materials and may serve as a general strategy for the performance enhancement of novel 2D optoelectronics.

Introduction

Piezo-phototronics represents a new class of devices that utilize strain-induced ionic piezopolarization to modulate the local energy band profile at the semiconductor interface, and thus the electro-optical process.[1–4] Compared with the conventional optoelectronics, performance of piezo-phototronics could be directly regulated with mechanical stimuli without applying any external gate bias. Following this novel principle, unprecedented device technologies have been developed, bringing significant impact to adaptive sensors, human–machine interfacing and smart robotics.[5] More importantly, the piezo-phototronic effect can be obviously achieved at room temperature without the requirement of ultra-low temperature or high vacuum, which greatly expands its application scenarios.[6] The primary focus in this area has been wurtzite structured semiconductors (*e.g.*, ZnO, GaN and CdS) with one-dimensional (1D) and thin-film morphology. Recently, the emergence of piezoelectric monolayers extends such a device concept into a new arena of two-dimensional (2D) materials, providing a fertile ground for the exploration of this effect at an atomic scale.[7–10]

Together with a favorable piezoelectric coefficient, strong light–matter interaction and superior mechanical properties, MoS_2 monolayer is considered as one of the most promising piezo-phototronic materials among the existing library of 2D crystals.[11–14] Compared with the 1D nanowires, a more prominent piezo-phototronic modulation effect in MoS_2 is expected because of its ability to sustain larger elastic strain and more complicated strain types (*e.g.*, uniaxial strain, biaxial strain and strain gradient).[15] Moreover, its thin-film morphology is compatible with the standard silicon semiconductor technology (*e.g.*, lithography, etching, metal/dielectric deposition, *etc.*), which may enable the realization of integrated 2D piezo-phototronics with high device density and reduced cost. With the advancement of chemical vapor deposition (CVD) techniques, the wafer-scale production of highly-oriented monolayer MoS_2 has been realized.[16] However, the inferior crystal quality has been an important obstacle hindering its application in high-performance piezo-phototronics. A relatively high intrinsic defect (*e.g.*, vacancy, adatom and antisite) density up to 10^{13} cm^{-2} has been observed in single-layer MoS_2, and the predominant category of defects in CVD-grown samples was determined to

[a] Key Laboratory of Material Physics of Ministry of Education, School of Physics and Engineering, Zhengzhou University, Zhengzhou 450001, P. R. China
[b] CAS Center for Excellence in Nanoscience, Beijing Key Laboratory of Micro-nano Energy and Sensor, Beijing Institute of Nanoenergy and Nanosystems, Chinese Academy of Sciences, Beijing 100083, P. R. China
[c] School of Nanoscience and Technology, University of Chinese Academy of Sciences, Beijing 100049, P. R. China
[d] School of Material Science and Engineering, Georgia Institute of Technology, Atlanta, Georgia 30332, USA. E-mail: zhong.wang@mse.gatech.edu

† Electronic supplementary information (ESI) available. See DOI: 10.1039/c9tc05337a

be the sulphur vacancy due to its low formation energy.[17–19] Being atomically thin, these charged sulphur vacancies tend to introduce localized impurity bands in MoS_2 and have a crucial impact on electronic/optical properties. In this regard, various approaches have been proposed to suppress the defect state in 2D materials with different repairing mechanisms.[20–22] In particular, as a crystal structure-determined property, it can be speculated that the piezoelectricity in 2D materials should be more susceptible to defects than that in the 3D bulk. From this viewpoint, defect engineering could be an effective strategy for piezoelectric property modulation and performance enhancement of 2D piezo-phototronics.

Here, we demonstrated the feasibility of piezo-phototronic effect enhancement in CVD-grown MoS_2 through defect repair. A poly(4-styrenesulfonate)-induced self-healing approach was adopted to repair the intrinsic sulphur vacancy, followed by chemical passivation with bis(trifluoromethane) sulfonimide (TFSI) to further reduce carrier density. Compared with flexible phototransistors fabricated with as-grown MoS_2 monolayer, a more prominent piezo-phototronic modulation impact was achieved after treatment. Under illumination of 19.1 μW cm^{-2} (532 nm wavelength), a 5.6-fold improvement of responsivity is demonstrated when a 0.42% uniaxial tensile strain is applied, and the optimized photoresponsivity reaches up to 339.2 A W^{-1}. This structure–property relationship research could advance our fundamental understanding of the piezo-phototronic effect in 2D materials and may serve as a reference for the artificial manipulation of the 2D piezoelectric property through defect engineering.

Results and discussion

The MoS_2 in our experiment was prepared *via* an oxygen-assisted CVD approach. The measured frequency separation between the in-plane E^1_{2g} and out-of-plane A_{1g} Raman vibration modes of MoS_2 is ~19.5 cm^{-1}, indicating its monolayer nature (Note 1 and Fig. S1, ESI†).[23,24] Compared with its bulk counterpart, monolayer MoS_2 becomes intrinsically piezoelectric due to the spontaneous breakdown of centrosymmetry. After transfer onto the SiO_2/Si substrate using a polymethyl methacrylate (PMMA)-assisted wet method, the MoS_2 was patterned into the shape of 'BINN' with electron-beam lithography and O_2 plasma, as shown in Fig. 1a. Fig. 1b and c show the photoluminescence (PL) intensity mapping of the as-grown and treated MoS_2 monolayer taken under the same conditions. An ~2-fold increase in peak intensity could be observed after the poly(4-styrenesulfonate)-induced defect repair and TFSI passivation, along with a blue shift of the peak energy by about 60 meV (Fig. 1d). Meanwhile, the FWHM (full width at half maximum) of the PL peak reduces from 42 nm to 17 nm. From the curve fitting analysis of the PL peak A shown in Fig. 1e, it is clear that the spectral weight of the negative trion (X^-) peak was dramatically suppressed, suggesting a significant decrease of background carrier concentration.[25,26] First, the sulfur vacancies could be healed by sulfur adatoms on the MoS_2 surface through a poly(4-styrenesulfonate)-induced hydrogenation process, thus reducing the donor state density and defect-mediated recombination process.[27,28] Meanwhile, as a Lewis acid, treatment with TFSI can effectively withdraw electrons

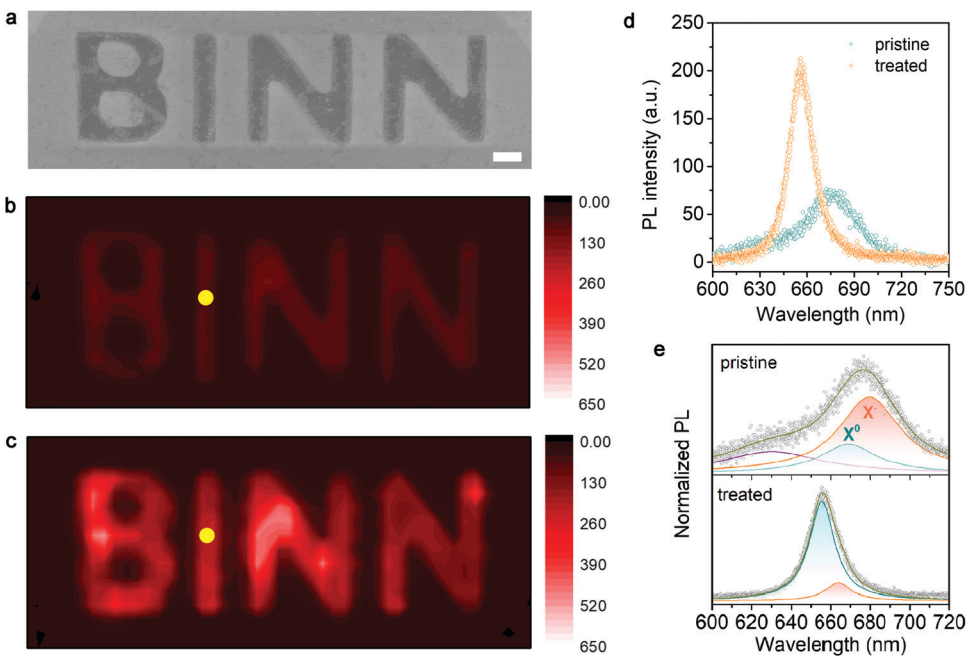

Fig. 1 (a) Scanning electron microscopy (SEM) image of monolayer MoS_2 patterned into the shape of 'BINN' with electron-beam lithography and O_2 plasma. Scale bar, 2 μm. PL intensity mapping of the as-grown MoS_2 monolayer (b) and treated MoS_2 (c) after defect repair and chemical passivation. (d) Comparison of PL spectra acquired from the same position in panels (b) and (c) highlighted with yellow circles, indicating an ~2-fold increase of peak intensity and a blue shift of peak energy by about 60 meV (from 1.83 to 1.89 eV). (e) Fitting analysis of the PL A peak by considering the contribution of trion X^- (orange) and exciton X^0 (cyan) peaks.

from MoS_2 by means of surface charge transfer to further reduce free carrier density.[29–32] Thus, the PL property of the treated MoS_2 monolayer is dominated by radiative exciton (X^0) recombination processes, leading to enhanced peak intensity and higher peak energy.

Fig. 2a shows the SEM image of the MoS_2 monolayer patterned into the shape of 'PIEZO' on a Au substrate. Kelvin probe force microscopy (KPFM) was employed to map the variation of MoS_2 work function before and after treatment, as shown in Fig. 2b and c. The contact potential difference (CPD) is defined as $(\varphi_{tip} - \varphi_{sample})/q$, where φ_{tip} and φ_{sample} represent work functions of the Au-coated AFM tip and MoS_2, respectively. From the cross-sectional profile taken from the same region highlighted with dashed lines, a decrease of CPD by ~50 meV could be observed after the treatment process (Fig. 2d). This indicates a larger work function of treated MoS_2 compared with the as-grown monolayer and its Fermi level moves far away from the conduction band (Fig. S2, ESI†). In addition, the measured work function of the Au substrate remains almost unchanged after the treatment process, which rules out the obvious existence of chemical residues. This indicates that the measured PL and KPFM change mainly originates from MoS_2 itself rather than the attachment of organic molecules. In order to further quantitatively evaluate the carrier density change, field-effect transistors were fabricated with a partially-treated MoS_2 monolayer on the SiO_2/Si substrate, as shown in the inset of Fig. 2e. After treatment, a clear right-shift of threshold voltage could be observed from the transfer characteristics, suggesting a decrease of intrinsic n-type doping concentration in CVD grown MoS_2 (Fig. 2e). The calculated electron density decreases from 8.58×10^{11} cm^{-2} to 1.56×10^{11} cm^{-2} after the treatment process (Fig. S3, ESI†), which is consistent with the PL and KPFM characterization results.

Fig. 3a shows the optical microscopy (OM) image of the two-terminal flexible MoS_2 phototransistor fabricated on the polyethylene terephthalate (PET) substrate. Due to the asymmetric modulation behavior of the piezo-phototronic effect, the metal–semiconductor–metal structure with a single Schottky contact was adopted in our experiment rather than the previously reported back-to-back Schottky junctions.[33,34] Moreover, considering the piezoelectric anisotropy in MoS_2, the asymmetric metal contacts were deliberately deposited parallel to the zigzag direction of the MoS_2 monolayer and the strain was precisely imposed along the armchair direction, which can be verified from its triangular morphology.[35,36] Electrical measurement of the fabricated device in the dark revealed excellent current rectification behavior, indicating the formation of a Pd–MoS_2 Schottky contact and Ohmic Cr–MoS_2 (Fig. S4, ESI†). The 532 nm laser with tunable optical power was illuminated over the device through an optical fiber (spot diameter ~300 μm).

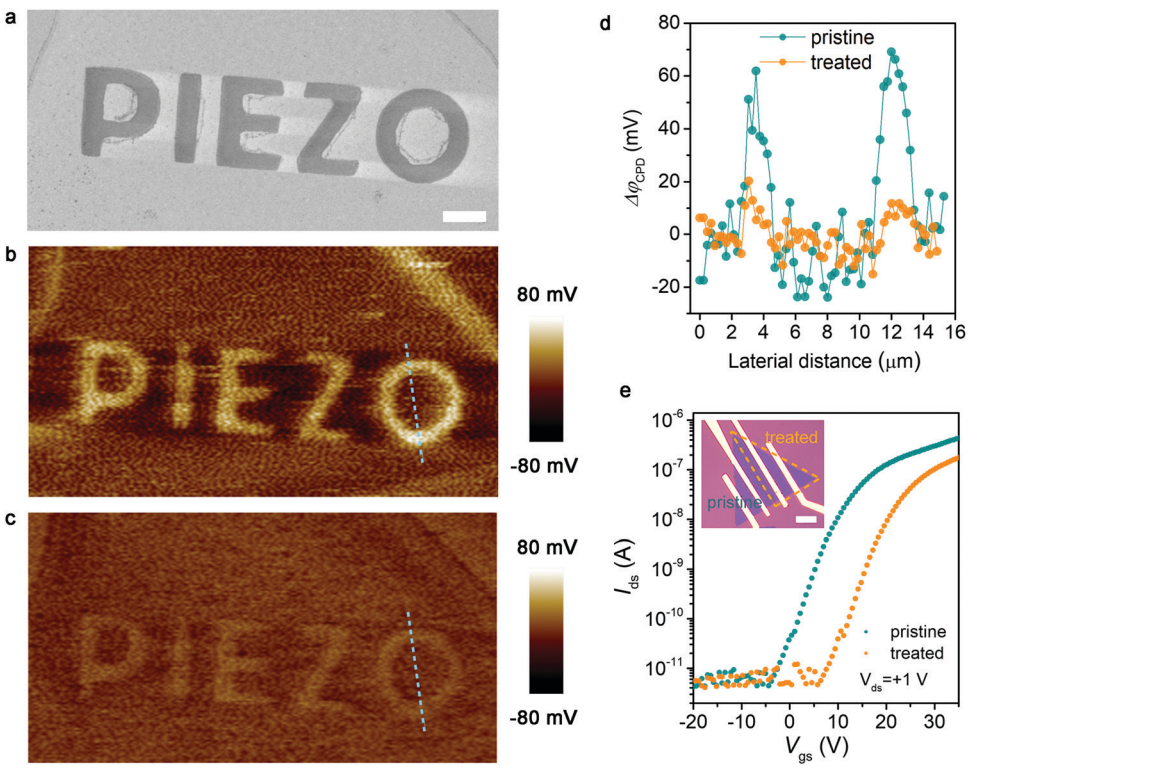

Fig. 2 (a) SEM image of MoS_2 monolayer patterned into the shape of 'PIEZO' on the Au substrate. Scale bar, 5 μm. (b and c) Corresponding surface potential image of MoS_2 before and after treatment; a Au-coated AFM tip was used for the KPFM measurement. (d) Comparison of the contact potential difference (V_{CPD}) profile taken from the same region in panels (b) and (c) highlighted with dashed lines. (e) Transfer characteristics of the pristine and locally-treated MoS_2 monolayer, suggesting a clear right-shift of the threshold voltage. The inset shows the optical microscopy image of fabricated transistors; scale bar, 10 μm.

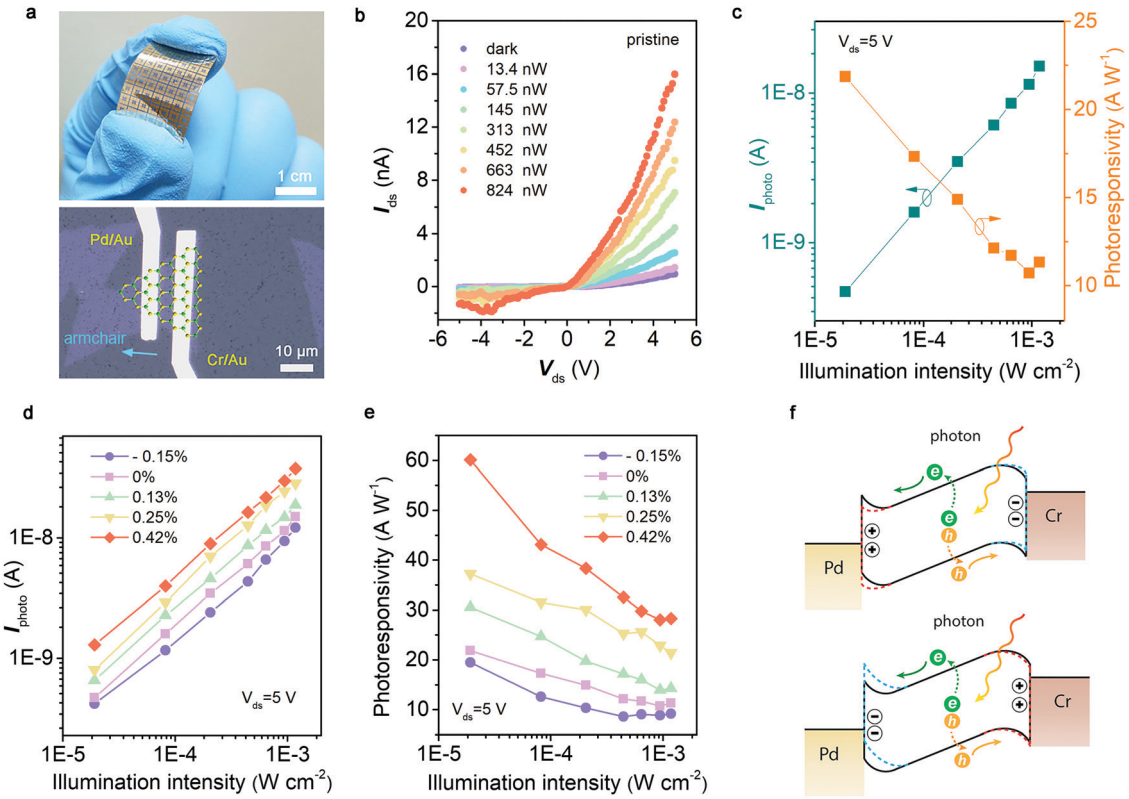

Fig. 3 (a) OM image of the flexible piezo-phototronic detector fabricated with monolayer MoS_2 on the PET substrate. Asymmetric electrical contacts were deposited parallel to the zigzag direction of MoS_2 to form a single Schottky junction. (b) Photoresponse of the device under strain-free conditions. (c) Calculated photocurrent and responsivity of the device at 5 V applied voltage. (d and e) Strain dependence of photocurrent and responsivity for different optical power intensities, suggesting the effective modulation of the photodetection property with strain. (f) Schematic of energy band diagrams for explaining the piezo-phototronic process. The red and blue dotted lines represent an interfacial energy band change under the influence of positive and negative piezopolarization charges, respectively.

Photoresponse of the devices fabricated with the as-grown MoS_2 under strain-free conditions is shown in Fig. 3b. A good linearity between the photocurrent I_{photo} ($I_{ds} - I_{dark}$) and illumination intensity could be observed across the whole measured range from μW cm^{-2} to mW cm^{-2}. The device photoresponsivity decreases with increasing illumination intensity (Fig. 3c), which may be attributed to the decrease of unoccupied states in the MoS_2 conduction band under higher optical power.[37] The maximum responsivity is about 21.8 A W^{-1} at a low illumination intensity of 19.1 μW cm^{-2} and 5 V applied voltage. A home-made experiment setup was used to characterize the piezo-phototronic process by measuring photoresponse under controlled light power and mechanical strain (Note 2 and Fig. S5, ESI†). The electrical transport shown in Fig. S6a (ESI†) indicates a significant strain dependency of dark current, suggesting the effective regulation of interface contact properties. Furthermore, modulation of device photodetection performance could also be observed from the photoresponse I_{ds}–V_{ds} curves under different static strains (Fig. S6b–f, ESI†). For all the illumination intensities, I_{photo} and the corresponding photoresponsivity increase with increasing tensile strain and decrease with compressive strain, as shown in Fig. 3d and e. Moreover, the modulation impact of strain on device performance is closely related to the optical power intensity and the effect attenuates with an increase of illumination intensity. At a low illumination intensity of 19.1 μW cm^{-2}, the responsivity reaches up to 60.1 A W^{-1} when a 0.42% tensile strain is applied, representing an ~1.8-fold improvement under strain-free conditions. However, the photoresponsivity only increases by ~1.4 times for 1.18 mW cm^{-2} high illumination. This is a typical characteristic of the piezo-phototronic effect due to the screening effect in piezoelectric semiconductors, which will be discussed in detail later. In addition, the increasing amplitude of photocurrent could also exclude the possible influence of strain-induced light absorption or carrier mobility change in MoS_2.[38]

The schematic energy band diagram explaining the observed piezo-phototronic behavior is shown in Fig. 3f. For 2H–MoS_2, the symmetry in the bulk with the D_{6h} point group is reduced to the D_{3h} group when thinned down to a monolayer, leading to the in-plane piezoelectric property. When a mechanical strain is applied along the polar direction, ionic polarization charges generated at the two edges of MoS_2 shift local electronic band bending and effectively manipulate carrier transport behavior across the junction interface. For the Pd–MoS_2–Cr device, the applied forward bias separates photo-generated excitons into free carriers, driving electron (hole) transfer across the Pd–MoS_2 Schottky barrier (Cr–MoS_2 Ohmic contact), giving rise

to the photocurrent. As the transport property at the Schottky junction is mainly determined by majority carriers and both Cr and Pd exhibit *n*-type contact behavior on the MoS_2 monolayer, the photodetection behavior in the fabricated devices is closely associated with the Pd–MoS_2 barrier characteristic.[39] Considering the crystal orientation of the used MoS_2, positive polarization charges are induced in the vicinity of the Pd–MoS_2 Schottky interface when tensile strains are introduced. These positive charges move the energy band downward and lower the Pd–MoS_2 interfacial barrier height. Meanwhile, the inclined energy-band within MoS_2 under a piezoelectric field functions as an applied external voltage and provides extra driving force to separate the photocarriers (the upper part of Fig. 3f).[40–42] Therefore, the extraction efficiency of photoexcited electrons in MoS_2 is promoted, leading to increased photocurrent and responsivity. In contrast, compressive strain-induced negative polarization charges shift the MoS_2 local energy band upward and increase the Pd–MoS_2 barrier height (the lower part of Fig. 3f). Thus, the injection of photo-induced electrons in MoS_2 into the Pd electrode across the Schottky interface is restrained and decreased photocurrent is observed. The polarization charges at the Cr–MoS_2 Ohmic contact may also affect local band-bending, but the modulation impact is supposed to be negligible due to the absence of the depletion region. This strain-gated photoelectric process in 2D piezoelectric materials offers an effective approach to modulate performance of optoelectronics, which may enable the design and implementation of novel flexible devices.

Fig. 4a shows the photoresponse of the fabricated devices under strain-free conditions after monolayer MoS_2 was treated. Compared with the result shown in Fig. 3b, it can be seen that the strong current rectification behavior is well preserved. Meanwhile, an increase of photocurrent could also be observed. This phenomenon may be interpreted from two combined effects: First, the dark current is greatly reduced (from 0.96 to 0.05 nA at 5 V bias) due to the decrease of background electron concentration after the treatment process. Moreover, the lower electron density suppresses the formation of trions, thus the separation of photogenerated excitons into free carriers under external applied bias is promoted. Second, repair of sulfur vacancies in the MoS_2 monolayer could lead to a substantial increase in photocarrier lifetime; consequently, the electron–hole recombination probability is reduced.[28,30] At a low illumination intensity of 19.1 μW cm^{-2} and 5 V bias, responsivity of the treated MoS_2 monolayer flexible phototransistor reaches up to 51.5 A W^{-1}, indicating an increase of 1.4 times over the pristine ones (Fig. S7, ESI†). Moreover, the good linearity between I_{photo} and illumination intensity is well preserved in the whole measured range. From the photoresponse curves of the treated MoS_2 device under different mechanical strains (Fig. 4b, c and Fig. S8, ESI†), a similar change in profile of photocurrent and responsivity could be observed (Fig. 4d and e). Under the same illumination intensity, the photocurrent (responsivity) increases with increasing tensile strain and decreases with compressive strain. Meanwhile, a similar optical

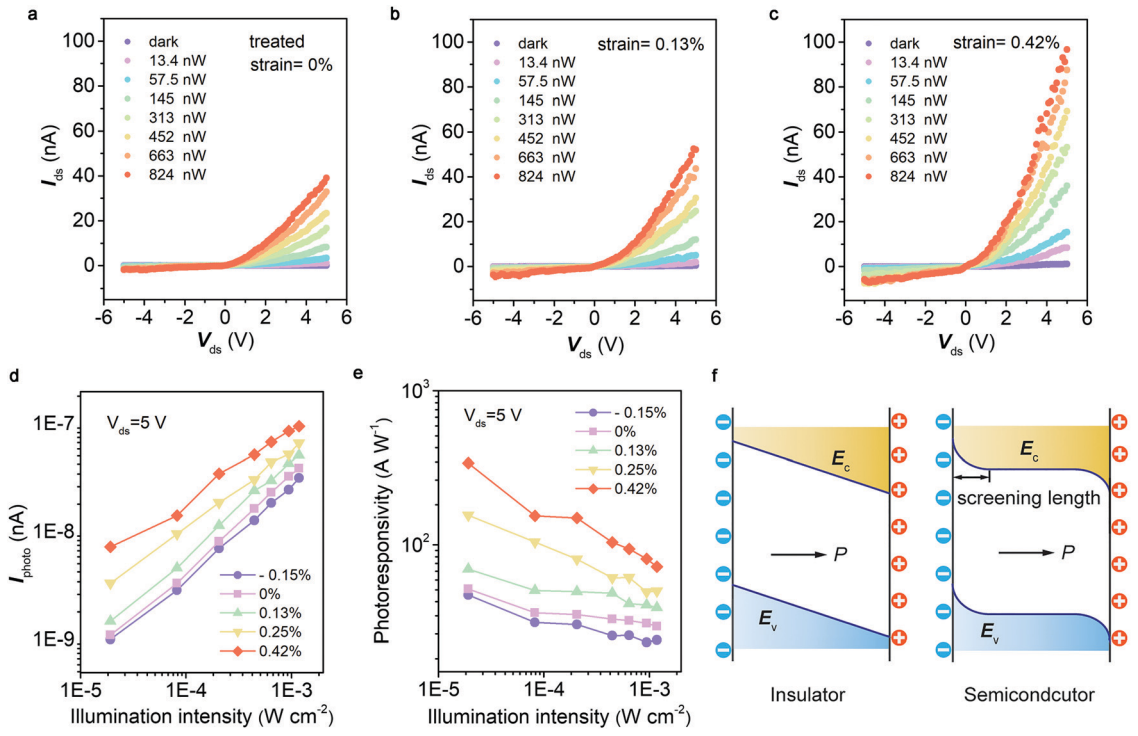

Fig. 4 (a) Photoresponse of the treated MoS_2 monolayer when no strain was applied. (b and c) Photodetection property of the treated MoS_2 under 0.13% and 0.42% tensile strains, indicating the effective modulation of performance with mechanical strain. (d and e) Strain dependence of photocurrent and responsivity for different optical power intensities. (f) Schematic showing the energy-band shift in insulators (without carriers) and semiconductors (moderate carrier density) when opposite polarization charges are generated at the two ends of the piezoelectric material.

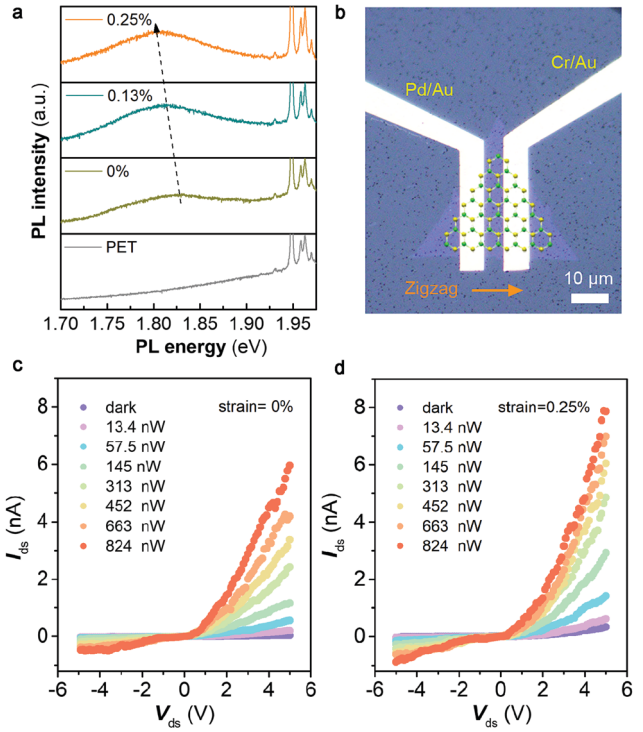

Fig. 5 (a) PL spectra of monolayer MoS_2 on the PET substrate under different tensile strains. (b) OM image of the flexible MoS_2 monolayer photodetector, with the asymmetric metal contacts deposited parallel to the armchair direction of MoS_2 and the strain applied along the zigzag direction. (c and d) Photoresponse of the fabricated devices under strain-free and 0.25% tensile strain.

power-dependent strain modulation was also observed in the treated devices. When a 0.42% tensile strain was applied, the responsivity increased from 51.5 A W^{-1} to 339.2 A W^{-1} at 19.1 μW cm^{-2} illumination, representing an ~5.6-fold improvement. This responsivity is relatively high for the flexible photodetector fabricated with CVD-grown MoS_2 monolayer.[43,44] Moreover, compared with the result shown in Fig. 3d and e, it can be seen that the modulation ability of the piezo-phototronic effect was greatly enhanced after the material treatment. The sulfur vacancy passivation and chemical treatment with TFSI can notably reduce charge carrier density in MoS_2; thus the screening effect is significantly weakened. As shown in Fig. 4f, for insulating piezoelectric materials, the electric field generated by strain-induced polarization charges tilts the whole electronic band in the material (the left part of Fig. 4f). However, for piezoelectric semiconductors with moderate free carrier concentrations, the energy band-bending was confined within the vicinity of material edges due to the appearance of the screening effect (right part of Fig. 4f).[45] This means that the ionic piezopolarization can be damped by the mobile charge carriers in semiconductors. As we have seen in plasmas and electrolytes, the Debye screening length is inversely related to charge carrier concentration, which is given by classic Poisson–Boltzmann theory.[46,47] Therefore, the high electron concentration in pristine CVD-grown MoS_2 can severely screen positive piezopolarization charges and weaken their modulation effect on Pd–MoS_2 interfacial band-bending. After treatment, more effective polarization charges are generated due to the passivation of defects and a decrease of carrier density leads to the increase of screening length, thus more pronounced modulation of device performance with the piezo-phototronic effect could be achieved.

Besides the piezo-phototronic effect, a change in the strain-induced band structure of MoS_2 may also contribute to the observed transport change in our devices. Fig. 5a shows the PL spectra of MoS_2 monolayer under different tensile strains. An ~26 meV red-shift of PL peak energy could be observed upon imposing a 0.25% tensile strain, which is in good agreement with the previous report.[14,48] By fitting the I_{ds}–V_{ds} curves in the dark with a thermionic emission equation, the calculated Schottky barrier height (SBH) change is ~66.4 meV when applying a 0.25% strain to the device, which is much larger than the band gap change (Fig. S9, ESI†). This demonstrates that the polar piezo-phototronic effect should dominate the performance modulation process in our devices. Furthermore, the crystal orientation-dependence of the piezo-phototronic effect in MoS_2 was also investigated, as shown in Fig. 5b. The asymmetric metal contacts were carefully deposited parallel to the armchair direction of MoS_2 monolayer and the strain was introduced along the zigzag direction. In this case, the positive (Mo) and negative (S) charge sites coincide, so there are negligible dipoles present in the strained material structure. Therefore, a relatively small photoresponse change was observed (Fig. 5c and d), which may originate from the piezo-resistive effect and band structure change.

Conclusions

In summary, suppression of the screening effect and thus the enhancement of piezo-phototronic modulation were achieved in CVD-grown monolayer MoS_2 through defect engineering. Due to the improved crystallization and decrease of free carrier concentration, the screening effect was greatly weakened. Compared with flexible phototransistors fabricated with as-grown MoS_2, a more significant piezo-phototronic modulation impact was achieved after treatment. At an illumination intensity of 19.1 μW cm^{-2}, a 5.6-fold improvement of photoresponsivity is demonstrated when applying 0.42% uniaxial tensile strain. The optimized responsivity reaches up to 339.2 A W^{-1}, which is relatively high for a flexible photodetector fabricated with CVD-grown MoS_2. This structure–property relationship research could advance our fundamental understanding of the piezo-phototronic effect in 2D materials. Meanwhile, it may also provide a reference for the artificial manipulation of 2D piezoelectricity at the atomic scale through defect engineering, site-specific doping or alloying.

Experimental section

Material transfer and characterization

Transfer of CVD grown MoS_2 onto the SiO_2/Si or PET substrate was accomplished using a PMMA-assisted wet method. In particular,

an accurate transfer platform (Metatest, E1-T) was used while fabricating the flexible MoS_2 phototransistor. Target MoS_2 with a specific direction was deliberately placed at the very center of the PET substrate, so that the substrate bending-induced strain can be effectively transferred to MoS_2 and reduce scattering of illumination light during the following piezo-phototronic test process. The Raman characterization and PL mapping were performed using a LabRAM HR Evolution Raman microscope with a 532 nm laser as the excitation source. Kelvin probe force microscopy (Bruker Dimension ICON) was employed to measure the surface potential change of MoS_2 before and after treatment.

Defect repair and chemical treatment of MoS_2

The poly(4-styrenesulfonate)-induced sulfur vacancy self-healing strategy was adopted for defect passivation of MoS_2 monolayer. First, the transferred MoS_2 was immersed in poly(3,4-ethylenedioxythiophene):poly(4-styrenesulfonate) (PEDOT:PSS) solution (Sigma-Aldrich, 1.0 wt% in H_2O) for 1.5 h at room temperature, which was accompanied by several washing processes involving deionized water to fully remove the PEDOT:PSS residuals. The MoS_2 was subsequently blow dried with Ar and baked on a 50 °C hotplate for 1 h to remove absorbed water molecules. Then, the repaired MoS_2 monolayer was immersed into a bis(trifluoromethane) sulfonimide solution (0.35 mg mL^{-1} in 1,2-dichloroethane) and kept on a hotplate at 100 °C for 5 min. Finally, the sample was blow dried and annealed at 100 °C for another 5 min.

Device fabrication and the piezo-phototronic process test

After the precise transfer of MoS_2 monolayer onto a flexible PET substrate, standard electron beam lithography (EBL) and thermal evaporation processes were performed twice to prepare the asymmetric electrical contacts. The Cr/Au (10 nm/50 nm) layer was deposited at one end of MoS_2 to form an Ohmic contact, and Pd/Au (10 nm/50 nm) was deposited at the other end to form a Schottky contact with MoS_2. Acetone was used for the lift-off process. All of the electrical transport and photoresponse properties were characterized by using a Keithley 4200 in a shielded probe station. The illumination power of 532 nm laser was subtly manipulated to avoid local heating of the polymer substrate. A home-made experimental setup was used to impose uniaxial elastic strain on MoS_2 by the bending of the PET substrate.

Conflicts of interest

There are no conflicts to declare.

Acknowledgements

This research was supported by the National Natural Science Foundation of China (Grant No. 51702017, 5151101243 and 51561145021), the National Key R & D Project from the Ministry of Science and Technology (2016YFA0202704), and the Beijing Municipal Science & Technology Commission (Z17110000 0317001, Z171100002017017 and Y3993113DF).

References

1 Z. L. Wang, *Nano Today*, 2010, **5**, 540–552.
2 Z. L. Wang, *Adv. Mater.*, 2012, **24**, 4632–4646.
3 W. Wu and Z. L. Wang, *Nat. Rev. Mater.*, 2016, **1**, 16031.
4 Y. Zhang, Y. Leng, M. Willatzen and B. Huang, *MRS Bull.*, 2018, **43**, 928–935.
5 Z. L. Wang, W. Wu and C. Falconi, *MRS Bull.*, 2018, **43**, 922–927.
6 A. Sohn, S. Choi, S. A. Han, T.-H. Kim, J. H. Kim, Y. Kim and S.-W. Kim, *Nano Energy*, 2019, **58**, 811–816.
7 P. Lin, C. Pan and Z. L. Wang, *Mater. Today Nano*, 2018, **4**, 17–31.
8 W. Wu, L. Wang, Y. Li, F. Zhang, L. Lin, S. Niu, D. Chenet, X. Zhang, Y. Hao, T. F. Heinz, J. Hone and Z. L. Wang, *Nature*, 2014, **514**, 470.
9 H. Zhu, Y. Wang, J. Xiao, M. Liu, S. Xiong, Z. J. Wong, Z. Ye, Y. Ye, X. Yin and X. Zhang, *Nat. Nanotechnol.*, 2014, **10**, 151.
10 P. Lin, L. Zhu, D. Li, L. Xu, C. Pan and Z. Wang, *Adv. Funct. Mater.*, 2018, **28**, 1802849.
11 K.-A. N. Duerloo, M. T. Ong and E. J. Reed, *J. Phys. Chem. Lett.*, 2012, **3**, 2871–2876.
12 M. Bernardi, M. Palummo and J. C. Grossman, *Nano Lett.*, 2013, **13**, 3664–3670.
13 H. Li, A. W. Contryman, X. Qian, S. M. Ardakani, Y. Gong, X. Wang, J. M. Weisse, C. H. Lee, J. Zhao, P. M. Ajayan, J. Li, H. C. Manoharan and X. Zheng, *Nat. Commun.*, 2015, **6**, 7381.
14 J. Feng, X. Qian, C.-W. Huang and J. Li, *Nat. Photonics*, 2012, **6**, 866.
15 D. Akinwande, C. J. Brennan, J. S. Bunch, P. Egberts, J. R. Felts, H. Gao, R. Huang, J.-S. Kim, T. Li, Y. Li, K. M. Liechti, N. Lu, H. S. Park, E. J. Reed, P. Wang, B. I. Yakobson, T. Zhang, Y.-W. Zhang, Y. Zhou and Y. Zhu, *Extrem. Mech. Lett.*, 2017, **13**, 42–77.
16 H. Yu, M. Liao, W. Zhao, G. Liu, X. J. Zhou, Z. Wei, X. Xu, K. Liu, Z. Hu, K. Deng, S. Zhou, J.-A. Shi, L. Gu, C. Shen, T. Zhang, L. Du, L. Xie, J. Zhu, W. Chen, R. Yang, D. Shi and G. Zhang, *ACS Nano*, 2017, **11**, 12001–12007.
17 J. Hong, Z. Hu, M. Probert, K. Li, D. Lv, X. Yang, L. Gu, N. Mao, Q. Feng, L. Xie, J. Zhang, D. Wu, Z. Zhang, C. Jin, W. Ji, X. Zhang, J. Yuan and Z. Zhang, *Nat. Commun.*, 2015, **6**, 6293.
18 J. Hong, C. Jin, J. Yuan and Z. Zhang, *Adv. Mater.*, 2017, **29**, 1606434.
19 J.-Y. Noh, H. Kim and Y.-S. Kim, *Phys. Rev. B: Condens. Matter Mater. Phys.*, 2014, **89**, 205417.
20 H. Qiu, T. Xu, Z. Wang, W. Ren, H. Nan, Z. Ni, Q. Chen, S. Yuan, F. Miao, F. Song, G. Long, Y. Shi, L. Sun, J. Wang and X. Wang, *Nat. Commun.*, 2013, **4**, 2642.
21 Z. Yu, Y. Pan, Y. Shen, Z. Wang, Z.-Y. Ong, T. Xu, R. Xin, L. Pan, B. Wang, L. Sun, J. Wang, G. Zhang, Y. W. Zhang, Y. Shi and X. Wang, *Nat. Commun.*, 2014, **5**, 5290.
22 Y. Meng, C. Ling, R. Xin, P. Wang, Y. Song, H. Bu, S. Gao, X. Wang, F. Song, J. Wang, X. Wang, B. Wang and G. Wang, *npj Quantum Mater.*, 2017, **2**, 16.

23 W. Chen, J. Zhao, J. Zhang, L. Gu, Z. Yang, X. Li, H. Yu, X. Zhu, R. Yang, D. Shi, X. Lin, J. Guo, X. Bai and G. Zhang, *J. Am. Chem. Soc.*, 2015, **137**, 15632–15635.
24 H. Li, Q. Zhang, C. C. R. Yap, B. K. Tay, T. H. T. Edwin, A. Olivier and D. Baillargeat, *Adv. Funct. Mater.*, 2012, **22**, 1385–1390.
25 K. F. Mak, K. He, C. Lee, G. H. Lee, J. Hone, T. F. Heinz and J. Shan, *Nat. Mater.*, 2012, **12**, 207.
26 S. Mouri, Y. Miyauchi and K. Matsuda, *Nano Lett.*, 2013, **13**, 5944–5948.
27 X. Zhang, Q. Liao, S. Liu, Z. Kang, Z. Zhang, J. Du, F. Li, S. Zhang, J. Xiao, B. Liu, Y. Ou, X. Liu, L. Gu and Y. Zhang, *Nat. Commun.*, 2017, **8**, 15881.
28 X. Zhang, Q. Liao, Z. Kang, B. Liu, Y. Ou, J. Du, J. Xiao, L. Gao, H. Shan, Y. Luo, Z. Fang, P. Wang, Z. Sun, Z. Zhang and Y. Zhang, *ACS Nano*, 2019, **13**, 3280–3291.
29 D.-H. Lien, S. Z. Uddin, M. Yeh, M. Amani, H. Kim, J. W. Ager, E. Yablonovitch and A. Javey, *Science*, 2019, **364**, 468–471.
30 M. Amani, D.-H. Lien, D. Kiriya, J. Xiao, A. Azcatl, J. Noh, S. R. Madhvapathy, R. Addou, S. Kc, M. Dubey, K. Cho, R. M. Wallace, S.-C. Lee, J.-H. He, J. W. Ager, X. Zhang, E. Yablonovitch and A. Javey, *Science*, 2015, **350**, 1065–1068.
31 H. Kim, D.-H. Lien, M. Amani, J. W. Ager and A. Javey, *ACS Nano*, 2017, **11**, 5179–5185.
32 M. Amani, P. Taheri, R. Addou, G. H. Ahn, D. Kiriya, D.-H. Lien, J. W. Ager, R. M. Wallace and A. Javey, *Nano Lett.*, 2016, **16**, 2786–2791.
33 J. Guo, R. Wen, J. Zhai and Z. L. Wang, *Sci. Bull.*, 2019, **64**, 128–135.
34 W. Wu, L. Wang, R. Yu, Y. Liu, S.-H. Wei, J. Hone and Z. L. Wang, *Adv. Mater.*, 2016, **28**, 8463–8468.
35 S. K. Kim, R. Bhatia, T.-H. Kim, D. Seol, J. H. Kim, H. Kim, W. Seung, Y. Kim, Y. H. Lee and S.-W. Kim, *Nano Energy*, 2016, **22**, 483–489.
36 A. M. van der Zande, P. Y. Huang, D. A. Chenet, T. C. Berkelbach, Y. You, G.-H. Lee, T. F. Heinz, D. R. Reichman, D. A. Muller and J. C. Hone, *Nat. Mater.*, 2013, **12**, 554.
37 Y. Xue, Y. Zhang, Y. Liu, H. Liu, J. Song, J. Sophia, J. Liu, Z. Xu, Q. Xu, Z. Wang, J. Zheng, Y. Liu, S. Li and Q. Bao, *ACS Nano*, 2016, **10**, 573–580.
38 G. H. Ahn, M. Amani, H. Rasool, D.-H. Lien, J. P. Mastandrea, J. W. Ager Iii, M. Dubey, D. C. Chrzan, A. M. Minor and A. Javey, *Nat. Commun.*, 2017, **8**, 608.
39 N. Kaushik, A. Nipane, F. Basheer, S. Dubey, S. Grover, M. M. Deshmukh and S. Lodha, *Appl. Phys. Lett.*, 2014, **105**, 113505.
40 R. Bao, Y. Hu, Q. Yang and C. Pan, *MRS Bull.*, 2018, **43**, 952–958.
41 P. Lin, L. Zhu, D. Li, L. Xu and Z. L. Wang, *Nanoscale*, 2018, **10**, 14472–14479.
42 J. Du, Q. Liao, M. Hong, B. Liu, X. Zhang, H. Yu, J. Xiao, L. Gao, F. Gao, Z. Kang, Z. Zhang and Y. Zhang, *Nano Energy*, 2019, **58**, 85–93.
43 H. Xu, J. Wu, Q. Feng, N. Mao, C. Wang and J. Zhang, *Small*, 2014, **10**, 2300–2306.
44 T.-Y. Kim, J. Ha, K. Cho, J. Pak, J. Seo, J. Park, J.-K. Kim, S. Chung, Y. Hong and T. Lee, *ACS Nano*, 2017, **11**, 10273–10280.
45 K. Chang, J. Liu, H. Lin, N. Wang, K. Zhao, A. Zhang, F. Jin, Y. Zhong, X. Hu, W. Duan, Q. Zhang, L. Fu, Q.-K. Xue, X. Chen and S.-H. Ji, *Science*, 2016, **353**, 274–278.
46 S. Sorgenfrei, C.-Y. Chiu, M. Johnston, C. Nuckolls and K. L. Shepard, *Nano Lett.*, 2011, **11**, 3739–3743.
47 L. M. B. C. Campos and F. J. P. Lau, *Phys. Plasmas*, 2014, **21**, 072109.
48 H. J. Conley, B. Wang, J. I. Ziegler, R. F. Haglund, S. T. Pantelides and K. I. Bolotin, *Nano Lett.*, 2013, **13**, 3626–3630.

